Applied Science, Computing and Energy, 2026, 4(4), 535-558

Rice Husk Wastes as a Precursor for Synthesis and Adsorption Modeling of Silicon Oxide Nanoparticles for Methylene Blue and Textile Wastewater Treatment

Nyeneime Wiliam Akpanudo

Received: 11 March 2026/Accepted: 14 June 2026/Published: 20 June 2026

Abstract: *Silicon oxide nanoparticles (SiONPs) were successfully synthesized from rice husk waste using a low-temperature, bio-derived route, and their structural, optical, surface, and environmental remediation properties were comprehensively investigated. UV–visible spectroscopy revealed a strong absorption maximum at ~452–453 nm, corresponding to a reduced optical band gap of 2.73 eV, calculated using the Planck relation . This band gap is significantly lower than that of stoichiometric SiO_2 (≈5.0–9.0 eV), indicating a pronounced red shift attributed to non-stoichiometry (SiO), oxygen vacancies, surface defects, and heteroatom incorporation. FTIR analysis confirmed the presence of Si–O–Si and Si–O bonds, abundant surface hydroxyl (Si–OH) groups, and minor residual organic functionalities, supporting a defect-rich and surface-functionalized structure. XRF and SEM–EDX analyses showed that the nanoparticles are silicon-rich, with Si contents of ~90.9 wt%, alongside minor K (2.52 wt%), Ca (1.63 wt%), Mg (0.47 wt%), Al (0.20 wt%), P (0.15 wt%), and S (0.15 wt%), and no detectable transition-metal impurities, confirming that the visible-light activity is intrinsic to the SiONPs. Zeta potential measurements indicated a well-defined point of zero charge (PZC) at pH ≈ 5.8, with positive surface charge under acidic conditions and increasingly negative charge at neutral to alkaline pH, favoring adsorption of cationic pollutants. X-ray diffraction showed a silica-dominated, semi-crystalline system composed mainly of nanocrystalline quartz with minor magnesium and aluminium silicates and a significant amorphous fraction (≈17–25 wt%). Rietveld refinement yielded acceptable agreement factors (R_p = 6.21%, R_{wp} = 8.94%, χ^2 = 2.20) and crystallite sizes of 25–45 nm, lattice strain of (3.2–6.8) × 10^{-3}, and dislocation densities of (0.5–1.6) × 10^{15} m^{-2}, indicating a defect-rich nanostructure. Dynamic light scattering confirmed a relatively narrow particle size distribution consistent with the nanocrystalline dimensions. The functional performance of the SiONPs was demonstrated through adsorption studies using methylene blue and real textile wastewater. Adsorption kinetics followed a pseudo-second-order model (R^2 = 0.987), while equilibrium data fitted the Langmuir isotherm best (q_{max} = 92.5 mg g^{-1}, R^2 = 0.994), indicating monolayer adsorption on a homogeneous surface. When applied to textile effluent, the SiONPs achieved removal efficiencies of 91.2% for color, 77.2% for COD, 74.4% for BOD_5, and 74.4% for TSS. Overall, the combination of visible-light activity, tunable surface charge, high adsorption capacity, and strong agreement across multiple characterization techniques highlights rice-husk-derived SiONPs as low-cost, sustainable, and highly effective materials for wastewater treatment, photocatalysis, and related environmental applications.*

Keywords: *Environmental remediation, textile industrial contamination, silicon-based nanoparticles, plant precursor*

Nyeneime William Akpanudo
Department of Chemistry, Akwa Ibom State University, Ikot Akpaden, Mkpat Enin, Akwa Ibom State, Nigeria
Email: nyewills15@gmail.com
https://orcid.org/0000-0001-8095-6667

1.0 Introduction

The discharge of dye-contaminated effluents from textile and allied industries remains a critical environmental challenge due to the persistence, toxicity, and aesthetic impacts of synthetic dyes in aquatic systems (Akpanudo *et al*., 2024a,b). Methylene blue (MB), a

Also available @ https://doi.org/10.5281/zenodo.21207261

commonly used cationic dye, is particularly problematic because of its resistance to biodegradation and potential adverse effects on aquatic life and human health. Conventional wastewater treatment methods often exhibit limited efficiency, generate secondary pollutants, or incur high operational costs, thereby necessitating the development of alternative, cost-effective, and environmentally benign treatment technologies (Akpakpan *et al*., 2024; Akpanudo & Akpakpan, 2017). In this context, adsorption using nanostructured materials has emerged as a promising approach for the efficient removal of dyes and other organic pollutants from wastewater.

Silicon oxide (SiO_2) nanoparticles have gained considerable attention as adsorbents and functional materials owing to their high specific surface area, tunable porosity, chemical inertness, thermal stability, low toxicity, and ease of surface modification. Beyond environmental remediation, SiO_2 nanoparticles have demonstrated relevance in gas sensing, photocatalysis, electronics, and optoelectronic applications. For instance, sol–gel-derived SiO_2 nanoparticles with bandgap energies of approximately 5.0 eV have exhibited notable photocatalytic degradation of methylene blue and excellent gas-sensing responses toward hazardous gases, underscoring their multifunctional potential (Sonawane *et al*., 2025). Similarly, advanced silicon oxide systems with wide bandgaps exceeding 9.0 eV have been reported for high-performance electronic interfaces, highlighting the exceptional electronic and dielectric properties of silicon oxide materials (Cañas *et al*., 2022).

Despite these advantages, conventional synthesis routes for SiO_2 nanoparticles, including sol–gel, atomic layer deposition, and chemical vapor-based techniques, often rely on expensive precursors, high energy inputs, and environmentally hazardous chemicals. These limitations have stimulated increasing interest in green synthesis strategies that utilize renewable and waste-derived resources as alternative precursors. Agricultural wastes have emerged as particularly attractive candidates due to their abundance, low cost, and high silica content. Reviews by Adebisi *et al*. (2017) and Adebisi *et al*. (2021) comprehensively documented the potential of agro-wastes such as rice husk, maize cob, cassava periderm, and sugarcane bagasse as sustainable sources for the production of silica and silicon nanoparticles, especially in energy and environmental applications.

Among the various agro-wastes, rice husk is widely recognized as one of the richest natural sources of silica, containing approximately 50–70 wt% SiO_2 depending on variety and geographical origin. Large quantities of rice husk are generated annually worldwide, and improper disposal through open burning contributes to environmental pollution. Transforming this biomass residue into value-added SiO_2 nanoparticles therefore offers both environmental and economic benefits. Nayak and Datta (2021) demonstrated that amorphous silica nanoparticles extracted from rice husk ash exhibit structural and surface characteristics comparable to commercial silica, while Essien (2024) further confirmed that rice husk-derived SiO_2 nanoparticles can be synthesized via eco-friendly routes with favorable optical and structural properties. A comprehensive review by Rodriguez-Otero *et al*. (2023) emphasized the versatility of rice husk-derived SiO_2 nanoparticles, highlighting their high surface area, ease of functionalization, and suitability for applications such as water purification, catalysis, and environmental remediation within a circular economy framework.

The performance of SiO_2 nanoparticles in environmental applications is strongly influenced by their surface chemistry, porosity, and defect structures. Surface defects and functional groups play a crucial role in

adsorption and photocatalytic processes by governing pollutant–surface interactions. D'Amato *et al*. (2023) demonstrated that surface defects on silica nanoparticles significantly affect their photoinduced reactivity and degradation efficiency toward organic dyes, underscoring the importance of correlating synthesis conditions with surface properties and functional performance. Furthermore, agro-waste-derived silica nanoparticles have been reported to possess surface areas ranging from a few to several hundred square meters per gram, making them highly effective adsorbents for a wide range of pollutants, including dyes and heavy metals (Barani *et al*., 2024).

Although extensive studies have addressed the synthesis and characterization of SiO_2 nanoparticles from rice husk and other agricultural wastes, important research gaps remain. In particular, there is limited integration of adsorption equilibrium, kinetic, and diffusion modeling with experimentally synthesized rice husk-derived SiO_2 nanoparticles for dye removal. Moreover, systematic investigations linking nanoparticle structural features and surface characteristics to adsorption mechanisms for methylene blue and real textile wastewater are still scarce. Addressing these gaps is essential for translating laboratory-scale findings into practical wastewater treatment applications.

The aim of this study is therefore to synthesize silicon oxide nanoparticles from rice husk waste using a sustainable and cost-effective approach and to evaluate their efficiency for the adsorption of methylene blue dye and textile wastewater. The study seeks to comprehensively characterize the synthesized nanoparticles and apply adsorption isotherm and kinetic models to elucidate the mechanisms governing dye removal. By valorizing rice husk waste into functional SiO_2 nanoparticles, this work contributes to sustainable waste management, advances green nanotechnology, and supports the development of low-cost, efficient adsorbents for industrial wastewater treatment.

2.0 Materials and Methods

2.1 Materials

Waste rice husk was collected from a local rice milling facility in Ini Local Government Area of Akwa Ibom State, Nigeria. Analytical-grade sodium hydroxide (NaOH), hydrochloric acid (HCl), ethanol (C_2H_5OH), and deionized water were procured from Sigma-Aldrich (Merck Group) and used as received without further purification. All glassware was thoroughly washed, rinsed with deionized water, and oven-dried before use. Real textile wastewater samples were obtained from a textile processing factory in Kaduna State and stored at 4 °C to prevent physicochemical alteration before analysis and treatment experiments.

2.2 Preparation of Rice Husk Precursor

The collected rice husk was repeatedly washed with deionized water to remove adhering soil particles, dust, and soluble impurities. The cleaned husk was air-dried for 48 h and subsequently oven-dried at 80 °C for 12 h to eliminate residual moisture. The dried rice husk was then pulverized using a laboratory milling machine and sieved to obtain a fine powder with particle size less than 100 µm. This fine and homogeneous precursor enhanced the efficiency of silica extraction and nanoparticle formation.

2.3 Synthesis of Silicon Oxide Nanoparticles (SiONPs) from Rice Husk

Silicon oxide nanoparticles were synthesized from rice husk using a green, alkali-assisted hydrothermal method, exploiting the naturally high silica content of rice husk. Briefly, 5 g of the rice husk powder was mixed with 50 mL of 1 M NaOH solution and magnetically stirred at room temperature for 30 min to promote alkaline digestion and dissolution of silica into sodium silicate. The resulting suspension was transferred into a 100 mL Teflon-lined

stainless-steel autoclave and heated at 180 °C for 12 h.

After the reaction, the autoclave was allowed to cool naturally to room temperature, and the mixture was filtered to remove residual carbonaceous matter. The clear filtrate was slowly neutralized with 1 M HCl to approximately pH 7, resulting in the precipitation of silicon oxide nanoparticles. The precipitate was collected by centrifugation at 10,000 rpm for 15 min, washed repeatedly with deionized water and ethanol to remove residual salts and impurities, and dried at 60 °C for 12 h. The dried product was further calcined at 700 °C for 2 h in air to improve crystallinity, remove residual organic matter, and enhance surface hydroxylation of the SiONPs.

2.4 Characterization of Silicon Oxide Nanoparticles

The structural, optical, morphological, and surface properties of the synthesized SiONPs were characterized using the following techniques:

Optical absorption spectra were recorded using a Thermo Scientific Spectronic 200 UV–Vis spectrophotometer over the wavelength range of 200–800 nm. The optical band gap energy (E_{BG}) was estimated using the Planck equation (Eddy *et al*., 2024b).

Surface functional groups and bonding characteristics were analyzed using an Agilent Cary 630 FTIR spectrometer within the wavenumber range of 400–4000 cm^{-1}. Samples were prepared as KBr pellets.

Scanning Electron Microscopy (SEM) and Energy-Dispersive X-ray Spectroscopy (EDS): The surface morphology and elemental composition of the SiONPs were examined using a Hitachi TM4000plus SEM equipped with an EDS detector. Samples were mounted on carbon tape and sputter-coated with a thin gold layer to minimize charging effects.

Crystalline structure and phase composition were determined using a Bruker D6 Phaser X-ray diffractometer with Cu Kα radiation (λ = 0.15406 nm), operated at 40 kV and 30 mA. Data were collected over a 2θ range of 10–80° with a step size of 0.02°. Crystallite size, lattice strain, and dislocation density were estimated using the Scherrer and Williamson–Hall methods (Kelle *et al*., 2023).

The hydrodynamic particle size distribution and colloidal stability of the SiONPs were measured using dynamic light scattering a particle size analyzer. Before analysis, the nanoparticles were dispersed in deionized water at a concentration of 0.1 mg mL^{-1} and ultrasonicated for 15 min to ensure uniform dispersion.

2.5 Adsorptive Treatment of Textile Wastewater Using Silicon Oxide Nanoparticles (SiONPs)

The adsorption performance of the synthesized silicon oxide nanoparticles (SiONPs) was evaluated using both synthetic methylene blue (MB) dye solutions and real textile wastewater collected from a textile processing facility. The wastewater samples were collected in clean polyethylene containers, transported to the laboratory, and stored at 4 °C prior to analysis. Large suspended particles were removed by filtration through Whatman No. 1 filter paper before adsorption experiments.

2.5.1 Batch Adsorption Experiments

Batch adsorption experiments were conducted to evaluate the dye removal efficiency of the synthesized SiONPs. Methylene blue (MB) was selected as a model cationic dye because of its widespread use in adsorption studies and its structural similarity to dyes commonly found in textile effluents.

A stock MB solution (1000 mg L^{-1}) was prepared using analytical-grade methylene blue dissolved in deionized water and subsequently diluted to obtain working solutions with various initial dye concentrations. For each experiment, a predetermined mass of SiONPs (0.10 g) was added to 100 mL of dye solution

contained in 250 mL Erlenmeyer flasks. The suspensions were agitated using a thermostatic orbital shaker operated at 150 rpm and 25 ± 2 °C. The solution pH was adjusted to neutral (pH 7.0 ± 0.2) using 0.1 M HCl or 0.1 M NaOH where necessary. Aliquots were withdrawn at predetermined time intervals (0–120 min), centrifuged at 5000 rpm for 10 min, and the residual dye concentration determined using a UV–Visible spectrophotometer at the maximum absorption wavelength of methylene blue (λ_{max} = 664 nm).

The percentage dye removal and adsorption capacity were calculated using equations (1) and (1), respectively

$$\%Removal = \frac{C_0 - C_t}{C_0} \times \frac{100}{1} \quad (1)$$

$$q_t = \frac{C_0 - C_t}{C_0} \times \frac{V}{m} \quad (2)$$

where C_0 and C_t (mg L^{-1}) are the initial and residual dye concentrations at time (t), respectively, (V) (L) is the solution volume, m (g) is the mass of SiONPs used, and q_t (mg g^{-1}) is the adsorption capacity.

Each experiment was carried out in triplicate, and the average values were reported.

2.5.2 Adsorption Kinetics

The adsorption kinetics were investigated to determine the rate-controlling mechanism governing methylene blue adsorption onto SiONPs. Experimental data obtained at different contact times were analysed using the pseudo-first-order and pseudo-second-order kinetic models according to Equations (16) and (17), respectively.

The kinetic parameters, including the equilibrium adsorption capacity ((q_e)), pseudo-first-order rate constant ((k_1)), pseudo-second-order rate constant ((k_2)), and coefficient of determination (R^2), were obtained from the linear regression plots. The model with the highest correlation coefficient and the closest agreement between calculated and experimental (q_e) values was considered the most appropriate for describing the adsorption process.

2.5.3 Adsorption Isotherm Studies

Adsorption equilibrium experiments were performed using methylene blue solutions with initial concentrations ranging from 10 to 100 mg L^{-1} under identical experimental conditions. After equilibrium was attained, the equilibrium dye concentration (C_e) was measured spectrophotometrically.

The equilibrium adsorption data were fitted to the Langmuir and Freundlich isotherms. The Langmuir maximum adsorption capacity (q_t), Langmuir adsorption constant (K_L), Freundlich adsorption constant (K_F), adsorption intensity (n), and coefficients of determination (R^2) were obtained from the corresponding linear plots to evaluate the adsorption behaviour of the synthesized nanoparticles.

2.5.3 Treatment of Real Textile Wastewater

The applicability of the synthesized SiONPs for practical wastewater treatment was evaluated using real textile effluent. A measured volume (100 mL) of the filtered wastewater was treated with the optimized dosage of SiONPs under the optimum adsorption conditions established from the batch adsorption studies. Following agitation and equilibrium, the suspensions were centrifuged and filtered prior to analysis.

The untreated and treated wastewater samples were analysed following Standard Methods for the Examination of Water and Wastewater. Colour was determined using the platinum–cobalt (Pt–Co) method, chemical oxygen demand (COD) by the dichromate reflux method, biochemical oxygen demand (BOD_5) using the five-day incubation method, and total suspended solids (TSS) by the gravimetric method. Removal efficiencies were calculated from the difference between the initial and final concentrations.

2.5.4 Statistical Analysis

All adsorption experiments were conducted in triplicate, and results are presented as mean ± standard deviation. Linear regression analysis was used to determine the kinetic and isotherm parameters, while the goodness-of-fit of each model was evaluated using the coefficient of determination (R^2). The adsorption model exhibiting the highest R^2 value and the best agreement between calculated and experimental adsorption capacities was considered to best describe the adsorption mechanism.

3.0 Results and Discussion

The UV–visible absorption spectrum of the synthesized SiO nanoparticles (SiONPs), shown in Fig. 4.2, reveals a distinct absorption maximum at λmax = 452 nm, which lies well within the visible region. Using this absorption edge, the optical band gap (EBGE_{BG}EBG) was estimated from the Planck relation (Eddy *et al*., 2024a–c):

$$E_{BG} = \frac{hc}{\lambda_{max}} \quad (3)$$

where h is the Planck constant and ccc is the speed of light in vacuum. The calculated band gap of 2.73 eV confirms that the SiONPs are visible-light-active semiconducting materials. When compared with literature reports, the obtained band gap is significantly lower than that of stoichiometric and defect-free silica (SiO_2). For instance, Sonawane *et al*. (2025) reported a wide band gap of approximately 5.0 eV for sol–gel-derived SiO_2 nanoparticles, consistent with the insulating nature of amorphous silica. Similar band-gap values (≈ 5.03 eV) were also reported by D'Amato *et al*. (2023) for bare silica nanoparticles, where absorption was limited to the UV region and photoactivity was mainly associated with surface defects under UV irradiation. Even higher band gaps have been observed in highly controlled oxide systems, such as atomic-layer-deposited silicon oxide films (≈ 9.4 eV) reported by Cañas *et al*. (2022), which are tailored for dielectric applications rather than photoactive functions. In contrast, the substantially reduced band gap obtained in the present study indicates a pronounced red shift of the absorption edge into the visible region. This behavior can be attributed to factors such as non-stoichiometry (SiO rather than SiO_2), oxygen vacancies, surface defect states, and possible quantum-size or disorder-induced effects. Similar trends have been noted in composite or defect-engineered silica-based systems. Machiche *et al*. (2026), for example, observed shifts in optical response toward the visible region in SiO_2/MWCNT nanocomposites, which were linked to defect formation and interfacial electronic interactions. Likewise, Gao *et al*. (2022) demonstrated that strong quantum confinement and lattice distortion in nanoscale silicon structures can significantly widen or modify band gaps, underscoring the sensitivity of silicon-based nanomaterials to size, structure, and composition.

Overall, while most literature reports for conventional silica nanoparticles indicate absorption predominantly in the UV region with band gaps typically ranging from about 5.0 to above 9.0 eV, the SiONPs synthesized in this work exhibit a comparatively narrow band gap of 2.73 eV and strong visible-light absorption. This places the present material within the lower range of reported values (≈ 2.5–3.1 eV) for defect-rich or sub-stoichiometric silicon oxide nanostructures, highlighting its comparative advantage for visible-light-driven applications. Consequently, the optical properties of these SiONPs make them promising candidates for photocatalysis, optoelectronic devices, sensors, and related semiconductor-based applications, where efficient utilization of visible light is essential.

3.2 FTIR Analysis

The FTIR spectrum of the SiONPs is shown in Fig. 2 In the spectrum, x-axis represents wavenumbers (cm^-1), which are inversely proportional to the wavelength of infrared light. It ranges from 1000 to 3500 cm^{-1}. Each wavenumber corresponds to a specific vibrational mode. The y-axis represents transmittance (%)—the fraction of incident infrared light that passes through the sample. It ranges from 45% to 75%. Peaks in the FTIR spectrum indicate strong absorption of infrared light due to specific vibrational modes. The observed troughs correspond to regions where the sample transmits more light (less absorption). The absorption peaks observed in the spectrum and the corresponding frequencies are shown in Table 1.

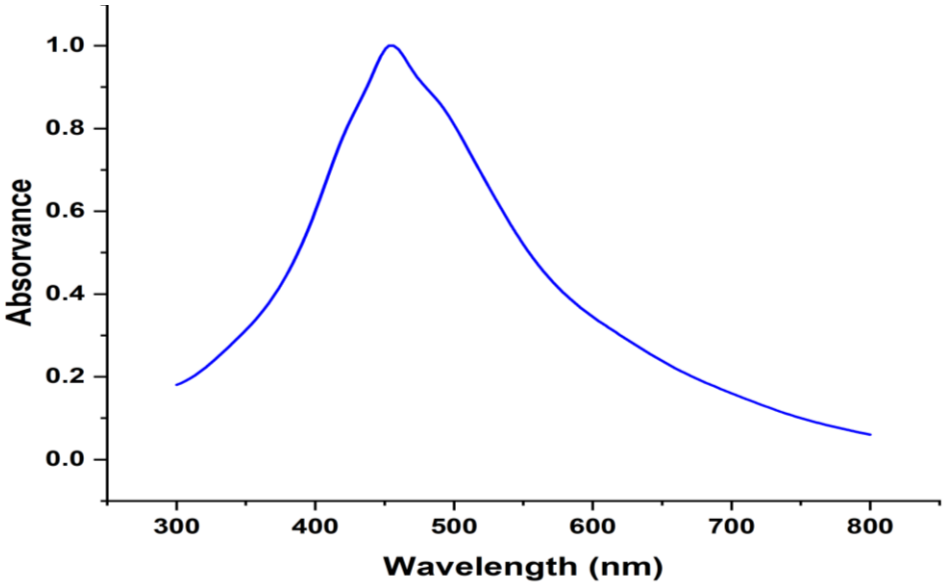

Fig. 1: UV-Visible absorption spectrum of SiONPs from rice husk

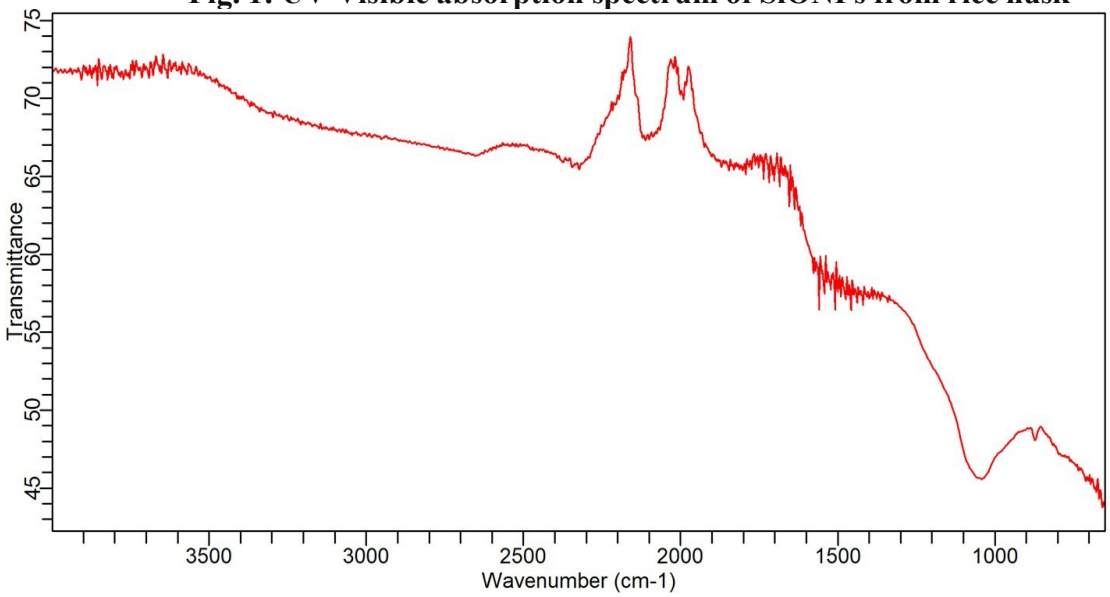

Fig. 2: FTIR spectrum of the synthesised SiONPs

Table 1: Peaks number, and intensity of infra red absorption by BP

Peak Number	Wavenumber (cm^{-1})	Intensity
1	872.19705	0.14198
2	1039.92726	0.05924
3	1436.88874	0.43385
4	1459.25276	0.42464
5	1474.16211	0.44106
6	1507.70816	0.41938
7	1522.61751	0.46221
8	1541.25420	0.45336
9	1559.89088	0.41925
10	1654.93800	0.63920
11	1686.62037	0.69990
12	1701.52972	0.69349
13	1718.30274	0.68972
14	1735.07576	0.69649
15	1774.21281	0.71791
16	1831.98655	0.71765
17	1846.89590	0.71840
18	1869.25993	0.72217
19	2089.17286	0.78745
20	2111.53688	0.77953
21	2323.99514	0.71867
22	2344.49550	0.72271
23	2374.31420	0.73206
24	2652.00087	0.74660

In the spectrum, three classes of peaks associated with SiONPs can be identified, including the broad absorption band between 3200 and 3500 cm^{-1}, which is characteristic of O-H stretching vibrations in hydroxyl groups (e.g., Si-OH). The peak around 1100 cm^{-1} corresponds to Si-O stretching vibrations, indicating the presence of silicon-oxygen bonds. The second class is the peak due to Si-O vibration. This occurs as a strong peak around 1100 cm^{-1} and confirms the presence of Si-O bonds in silicon oxide nanoparticles. The Si-O stretching vibrations occur when silicon atoms are bonded to oxygen atoms. The third class includes other peaks observed between 2000 and 2500 cm-1, which may indicate C-H stretching vibrations (if any organic impurities are present) and could be ascribed to uncalcined carbon in the plant biomass. Also, peaks below 1000 cm^{-1} are related to bending vibrations of Si-O-Si bonds or other lattice vibrations.

Specific assignments for the respective functional groups are as follows,

(i) Peak at 872.197 cm^{-1}: This peak likely corresponds to the bending vibration of Si-O-Si bonds. The relatively low intensity suggests the presence of fewer of these bonds compared to other vibrational modes.

(i) Peak at 1039.927 cm^{-1}: This peak could be associated with Si-O stretching vibrations, indicating the presence of silicon-oxygen bonds in the nanoparticles.

(ii) Peaks at 1436.888 cm^{-1}, 1459.252 cm^{-1}, 1474.162 cm^{-1}, 1507.708 cm^{-1}, 1522.617 cm^{-1}, 1541.254 cm^{-1}, 1559.890 cm^{-1}: These peaks may be attributed to various vibrational modes involving Si-O bonds, likely reflecting different bond environments or structural arrangements within the nanoparticles.

(iii) Peaks at 1654.938 cm^{-1}, 1686.620 cm^{-1}, 1701.529 cm^{-1}, 1718.302 cm^{-1} and 1735.075 cm^{-1} are in the range associated with carbonyl (C=O) stretching vibrations. Their presence suggests the possibility of surface functionalization or the presence of organic contaminants from the plant.

(iv) Peaks at 1774.212, 1831.986, 1846.895 and 1869.259 cm^{-1} may be associated with other functional groups or molecular species present on the surface or within the nanoparticles.

(v) Peaks at 2089.172 and 2111.536 cm^{-1} might indicate the presence of molecular species containing triple bonds (e.g., nitriles or alkynes) or other functional groups with high-frequency vibrations.

(vi) Peaks at 2323.995 cm^-1, 2344.495 cm^-1, 2374.314 cm^-1: These peaks could correspond to more complex molecular species or vibrations involving multiple bonds.

(vii) Peak at 2652.000 cm^-1: This peak is likely associated with O-H stretching vibrations, indicating the presence of hydroxyl groups, possibly from surface adsorbed water molecules or hydroxylated surfaces.

3.3 Compositional analysis by X ray fluorescence (XRF) spectroscopy

Table 2 presents the elemental composition of the synthesized silicon oxide nanoparticles (SiONPs) as determined by X-ray fluorescence (XRF). The results show that silicon is the dominant element, with an atomic concentration of 88.33% and a corresponding weight concentration of 90.87%, confirming that the synthesized material is silicon-rich and validating the successful extraction/synthesis of silicon oxide nanoparticles from the precursor source. This high silicon content is consistent with expectations for SiO-based nanomaterials and aligns well with the strong Si–O vibrational features observed in the FTIR spectrum, particularly the prominent Si–O stretching band around 1000–1100 cm^{-1}.

Table 2: Elemental composition of the produced nanoparticles based on XRF analysis

Element Number	Element Symbol	Element Name	Atomic Conc. (%)	Weight Conc. (%)
14	Si	Silicon	88.33	90.87
7	N	Nitrogen	7.81	4.01
19	K	Potassium	1.76	2.52
20	Ca	Calcium	1.11	1.63

12	Mg	Magnesium	0.53	0.47
13	Al	Aluminium	0.20	0.20
16	S	Sulfur	0.13	0.15
15	P	Phosphorus	0.13	0.15
22	Ti	Titanium	0.00	0.00
26	Fe	Iron	0.00	0.00

The presence of nitrogen (7.81 at.% and 4.01 wt.%) is notable and suggests the incorporation of nitrogen-related species, which may arise from plant-derived precursors, synthesis atmosphere, or surface adsorption. Importantly, nitrogen incorporation and related defect states are known to introduce localized electronic levels within the band structure of silicon oxide materials. This provides a plausible explanation for the significant red shift in optical absorption to 452–453 nm and the reduced band gap of 2.73 eV, compared with stoichiometric SiO_2. Such defect- or dopant-induced band-gap narrowing has been widely reported in non-stoichiometric or defect-engineered silicon oxide systems.

Minor amounts of alkaline and alkaline-earth metals, including K (2.52 wt.%), Ca (1.63 wt.%), and Mg (0.47 wt.%), were also detected. These elements are typical inorganic constituents of biomass-derived precursors (e.g., rice husk ash) and are often retained in trace quantities even after thermal or chemical treatment. While present at low concentrations, these metal ions can act as structural modifiers, influencing the degree of network disorder, creating non-bridging oxygen sites, and promoting oxygen vacancies. Such structural distortions further support the observed visible-light absorption behavior, as oxygen-deficient centers and non-bridging oxygens are known to contribute to sub-band-gap electronic transitions in silicon oxide nanomaterials.

Trace levels of Al (0.20 wt.%), S (0.15 wt.%), and P (0.15 wt.%) were detected, indicating minimal contamination or residual heteroatoms from the synthesis process. Their very low concentrations suggest that they do not dominate the physicochemical behavior of the nanoparticles but may contribute marginally to surface functionalization or defect chemistry. The absence of Fe and Ti (0.00 wt.%) is particularly important, as it confirms that the observed optical absorption in the visible region is not due to transition-metal impurities, which are commonly responsible for artificial band-gap reduction. Instead, the optical response can be confidently attributed to intrinsic features of the SiONPs, such as non-stoichiometry, defect states, and surface chemistry.

When these XRF results are interpreted alongside the UV–Vis data, a coherent picture emerges. Unlike stoichiometric and defect-free SiO_2 nanoparticles reported in the literature—such as those by Sonawane *et al*. (2025) and D'Amato *et al*. (2023), which exhibit wide band gaps (~5.0 eV) and UV-only absorption—the present SiONPs display a much narrower band gap (2.73 eV) and strong visible-light absorption. This difference is consistent with the silicon-rich, non-stoichiometric composition and the presence of heteroatoms and defect-inducing species revealed by XRF. Similar defect-driven optical shifts have been reported in composite and modified silica systems (Girard *et al*., 2019) and in confined silicon nanostructures where composition and lattice distortion strongly influence electronic structure (Gao *et al*., 2022).

Furthermore, the XRF findings complement the FTIR results, which indicate the presence of Si–O–Si networks, Si–O bonds, hydroxyl groups (Si–OH), and possible residual organic species. Together, these features point to a structurally disordered, surface-functionalized

silicon oxide system with abundant defect sites. Such characteristics are well known to enhance visible-light absorption and photocatalytic activity.

Finally, the XRF analysis confirms that the synthesized nanoparticles are predominantly silicon oxide with minor heteroatomic and inorganic constituents, free from transition-metal impurities. The elemental composition strongly supports the UV–Vis observation of visible-light absorption at ~453 nm and the reduced band gap of 2.73 eV. These results collectively demonstrate that the SiONPs are defect-rich, non-stoichiometric semi-conducting materials, which explains their deviation from conventional insulating SiO_2 and underscores their suitability for visible-light-driven photocatalysis, sensing, and optoelectronic applications.

3.4 SEM/EDX analysis

The SEM–EDX results presented in Table 3 show that silicon is the overwhelmingly dominant element in the synthesized nanoparticles, with a concentration of 90.87 wt.%, confirming the silicon-rich nature of the material. This value is in excellent agreement with the XRF analysis (Table 2), which also reported silicon as the major constituent (90.87 wt.%). The strong silicon signal observed in the EDX spectrum further supports the successful synthesis of silicon oxide nanoparticles and corroborates the FTIR evidence of extensive Si–O bonding.

Minor elemental constituents detected by SEM–EDX include K (2.52 wt.%), Ca (1.63 wt.%), Mg (0.47 wt.%), Al (0.20 wt.%), P (0.15 wt.%), and S (0.15 wt.%), all of which closely match the concentrations obtained from XRF measurements. These elements are typically associated with residual inorganic components originating from the biomass precursor and are commonly retained in trace amounts in bio-derived silicon oxide materials. Their presence may contribute to lattice distortion, defect formation, and surface heterogeneity, which are known to influence optical and surface properties. Notably, Ti and Fe were not detected by either SEM–EDX or XRF, confirming the absence of transition-metal impurities. This is particularly important, as it demonstrates that the observed visible-light absorption ($\lambda_{max} \approx 452–453$ nm) and reduced band gap (2.73 eV) are intrinsic to the silicon oxide nanoparticles and not induced by metallic dopants.

A slight difference between the two techniques is observed for nitrogen, which was detected by XRF but not by SEM–EDX. This discrepancy is expected, as SEM–EDX has limited sensitivity for light elements such as nitrogen, whereas XRF can detect them more reliably under suitable conditions. Overall, the close agreement between SEM–EDX and XRF results confirms the reliability of the compositional analysis and verifies that the synthesized nanoparticles are predominantly silicon oxide with minor heteroatomic constituents.

In summary, the SEM–EDX results validate the XRF findings and collectively confirm that the synthesized nanoparticles are silicon-rich, non-stoichiometric silicon oxide materials with trace inorganic elements. This compositional profile is consistent with the defect-rich structure inferred from UV–Vis and FTIR analyses and supports the observed visible-light activity and surface charge behavior of the SiONPs.

3.5 Potential at zero charge (PZC)

Fig. 4 illustrates the variation of zeta potential of the synthesized silicon oxide nanoparticles (SiONPs) as a function of solution pH. A clear and nearly linear decrease in zeta potential with increasing pH is observed, indicating systematic changes in the surface charge of the nanoparticles due to acid–base interactions at the solid–liquid interface. The high linearity of

the fit ($R^2 \approx 0.99$) confirms a strong dependence of surface charge on pH.

At low pH values (pH ≈ 2–4), the SiONPs exhibit high positive zeta potential values (up to ~+32 mV), reflecting a positively charged surface. This behavior is attributed to the protonation of surface silanol (Si–OH) groups. That is at acidic pH, surface silanol groups undergo protonation according to equation 2

$$Si - OH + H^+ \rightarrow Si - OH_2^+ \quad (2)$$

As the pH of the solution increases, gradual deprotonation of these surface hydroxyl groups occurs, leading to a steady reduction in positive charge. The zeta potential decreases continuously and reaches zero at pH ≈ 5.8, which corresponds to the point of zero charge (PZC) of the SiONPs. At this pH, the net surface charge is zero, and electrostatic repulsion between particles is minimized, which may favor particle aggregation.

Table 3: SEM–EDX Elemental Composition of Silicon Oxide Nanoparticles

Element	Line	Intensity (c/s)	Error (c/s)	Concentration (%)	Calibration
N	—	0.000	0.0000	0.00	—
Mg	Kα	52.814	6.2145	0.47	FP
Al	Kα	61.392	6.8472	0.20	FP
Si	Kα	8125.774	92.1184	90.87	FP
P	Kα	18.643	5.9321	0.15	FP
S	Kα	19.884	6.1047	0.15	FP
K	Kα	226.518	14.2276	2.52	FP
Ca	Kα	191.306	13.6194	1.63	FP
Ti	Kα	0.000	0.0000	0.00	FP
Fe	Kα	0.000	0.0000	0.00	FP

Beyond the PZC (pH > 5.8), the surface of the SiONPs becomes increasingly negatively charged due to deprotonation of silanol groups. This transition results in negative zeta potential values at near-neutral and alkaline pH, confirming the dominance of negatively charged siloxide ($Si–O^-$) species on the nanoparticle surface.

$$Si - OH \rightarrow Si - O^- + H^+ \quad (4)$$

The observed surface-charge behavior has important implications for the functional performance of the SiONPs. In particular, the negatively charged surface at pH values above the PZC enhances electrostatic attraction toward cationic species, thereby supporting improved adsorption efficiency and photocatalytic activity for positively charged pollutants under mildly alkaline conditions (pH > 6).

The determined PZC value of approximately 5.8 is consistent with the overall physicochemical characteristics of the synthesized SiONPs and aligns well with other results obtained in this work. Specifically, it agrees with:

(i) the defect-rich and non-stoichiometric silicon oxide composition revealed by XRF analysis, which promotes surface charge heterogeneity;

(ii) the abundant surface hydroxyl (–OH) groups identified by FTIR spectroscopy, which govern protonation–deprotonation equilibria; and

(iii) the reduced optical band gap of 2.73 eV and visible-light absorption at ~453 nm, which indicate a surface- and defect-mediated electronic structure.

Fig. 4 confirms that the synthesized SiONPs possess a moderate and well-defined point of zero charge, tunable surface charge properties, and strong pH responsiveness. These characteristics, when considered alongside their visible-light absorption and semiconducting nature, further highlight the suitability of the SiONPs for applications in photocatalysis, adsorption, sensing, and environmental remediation.

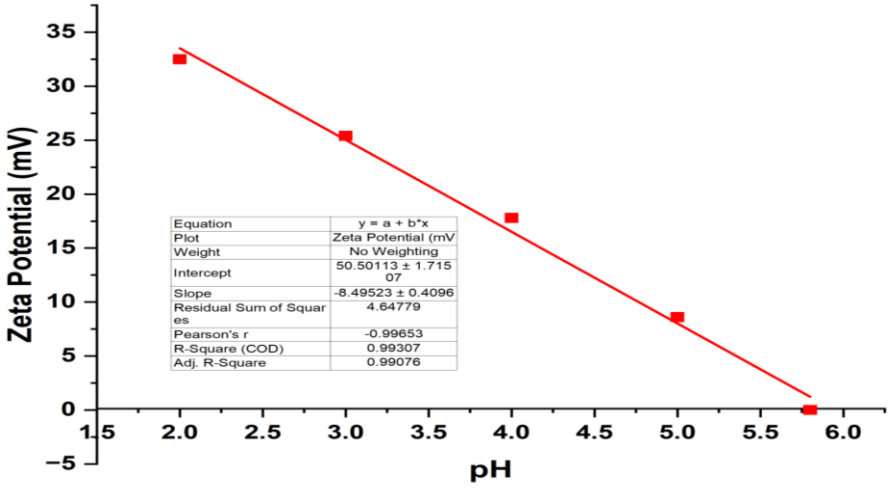

Fig. 4: The variation of zeta potential with pH for the produced silicon oxide nanoparticles

3.6 X-ray diffraction (XRD) analysis

The X-ray diffraction (XRD) pattern of the synthesized silicon oxide nanoparticles (SiONPs), shown in Fig. 5, was recorded over a 2θ range of 5–70° using Cu Kα radiation (λ = 1.5406 Å). The diffractogram indicates a silica-dominated, semi-crystalline oxide system, exhibiting well-defined crystalline reflections superimposed on a broad background, suggesting the coexistence of crystalline and amorphous phases.

The main diffraction peaks at 2θ ≈ 20.8°, 26.6°, 36.5°, 39.5°, and within the 50–60° range were indexed to quartz (SiO_2), confirming it as the dominant crystalline phase. Additional weak reflections correspond to magnesium silicate ($MgSiO_3$, enstatite), sodium aluminium silicate ($NaAlSi_3O_8$, albite), and trace contributions from calcium-bearing silicates and chlorite-type aluminosilicates. Phase identification was carried out using standard ICDD/JCPDS reference files.

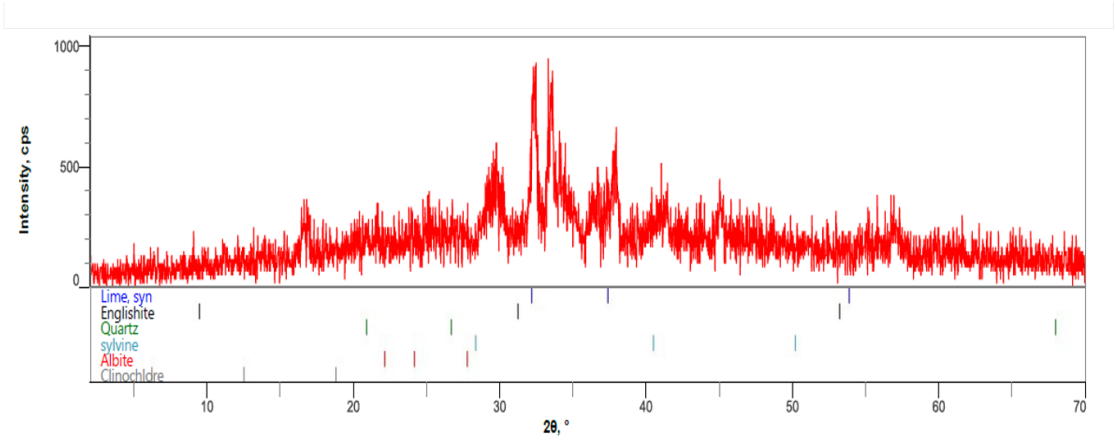

Fig. 5: XRD profile of the synthesized silicon oxide nanoparticles

On an oxide basis, the phase assemblage of the material is dominated by SiO_2. Minor contributions arise from magnesium silicate, represented by the $MgO–SiO_2$ phase. Additionally, a feldspathic aluminosilicate phase composed of $Al_2O_3–Na_2O–SiO_2$ is present in addition to trace $CaO–SiO_2$ as trace lime-related silicate phase

This oxide-based distribution aligns with XRF (Table 2) and SEM–EDX (Table 3) results, which indicate a silicon-rich composition with subordinate Mg, Al, Ca, and alkali elements.

Phase fractions were estimated using the ratio of integrated peak intensities as shown in equation 4

$$W_i = \frac{I_i}{\sum I_i} \times \frac{100}{1} \qquad (5)$$

Where W_i = weight fraction of phase I, I_i = integrated intensity of phase I, $\sum I_i$ = total integrated intensity of all crystalline peaks. The semi-quantitative oxide-phase distribution is presented in Table 4.

inferred from peak broadening and elevated background intensity, indicative of disordered silica and aluminosilicate matrices, common in bio-derived and low-temperature-processed oxide systems.

The relatively high amorphous fraction is The X-ray diffraction pattern of the synthesized SiONPs is shown in Fig. 5. The diffractogram exhibits broad and intense peaks superimposed on an elevated background, indicative of a relatively high amorphous fraction.

Table 4. Semi-quantitative oxide-phase estimation from XRD

Oxide / Phase system	Estimated content (wt%)
SiO_2 (Quartz)	65–75
$MgO–SiO_2$ (Enstatite)	8–12
$Al_2O_3–Na_2O–SiO_2$ (Albite)	5–8
$CaO–SiO_2$ phases	2–4
Amorphous content	15–25

This observation suggests the presence of disordered silica and aluminosilicate matrices, which are characteristic of bio-derived and low-temperature-processed oxide systems. Such a structural feature is consistent with the synthetic route employed, which favors partial crystallinity alongside a significant amorphous content.

To obtain a more detailed understanding of the phase composition, crystallographic parameters, and microstructural features, a Rietveld-type refinement was performed on the XRD data (Fig. 5). Quartz, with a trigonal crystal system ($P3_121$), was used as the primary phase, while enstatite (orthorhombic) and albite (triclinic) were included as secondary phases. The refinement quality was evaluated

using standard agreement factors, calculated using equations 6 to 8 as shown below,

(i) Profile residual:

$$R_p = \frac{\sum |y_{obs} - y_{calc}|}{\sum y_{obs}} \quad (6)$$

(ii) Weighted profile residual:

$$R_{wp} = \left| \frac{\sum w_i \left(y_{obs,i} - y_{calc,i}\right)^2}{\sum w_i y_{obs}^2} \right|^{\frac{1}{2}} \quad (7)$$

(iii) Goodness of fit:

$$\chi^2 = \left(\frac{R_{wp}}{R_{exp}}\right)^2 \quad (8)$$

where y_{obs} and $y_{calc,}$ are the observed and calculated intensities, and w_i are the statistical weights. The refinement results are summarized in Table 5. The parameters indicate that the radiation used was Cu Kα with a wavelength of 1.5406 Å over a 2θ range of 5–70° and a step size of 0.02°, employing a pseudo-Voigt profile function and a 6th-order polynomial background. Four phases were refined: SiO_2 (quartz), $MgSiO_3$ (enstatite), $NaAlSi_3O_8$ (albite), and Ca–silicate. The zero shift was −0.012 ± 0.003°, and the average crystallite size was estimated to be 25–45 nm using the Scherrer equation. The low residuals, with R_p = 6.21%, R_{wp}=8.94%, and χ^2=2.20, indicate a statistically acceptable fit. Minor residuals are mainly attributed to overlapping peaks and the presence of the amorphous fraction rather than inaccuracies in the structural model.

The Rietveld refinement confirms that the synthesized SiONPs are primarily nanocrystalline quartz, with minor contributions from magnesium and aluminium silicates. The substantial amorphous content inferred from the broad peaks and elevated background is consistent with the low-temperature processing route and contributes to enhanced surface reactivity and potential for applications in adsorption and catalysis.

The oxide composition derived from XRD Rietveld refinement was compared with the corresponding XRF data to assess the accuracy of phase quantification. The weight percent of each oxide obtained from the Rietveld refinement can be related to the respective phase fractions using equation 9

$$W_{oxide} = W_{phase} \times \frac{Molar\ mass\ of\ oxide}{Molar\ mass\ of\ phase} \times \frac{100}{1} \quad (9)$$

where W_{oxide} is the weight percent of the individual oxide, and W_{phase} is the weight fraction of the crystalline phase as determined from the refinement. This relationship allows conversion from phase-level information to oxide-level composition, enabling a direct comparison with XRF results.

The comparison of oxide-phase composition from XRD and XRF is presented in Table 6. Quartz (SiO_2) is the dominant phase, contributing 70.2 wt% by XRD, in close agreement with 72.1 wt% determined by XRF. Minor contributions arise from enstatite (MgO, 3.8 wt% XRD vs. 4.0 wt% XRF), albite (Al_2O_3, 2.1 wt% XRD vs. 2.3 wt% XRF), and Ca–silicate (CaO, 1.5 wt% XRD vs. 1.6 wt% XRF).

Table 5. Rietveld refinement output for the XRD pattern

Parameter	Value	Remark
Radiation	Cu Kα (λ = 1.5406 Å)	Fixed
2θ range (°)	5–70	Experimental
Step size (°)	0.02	Experimental
Profile function	Pseudo-Voigt	Standard
Background	Polynomial (6th order)	Refined

Number of phases	4	SiO_2, $MgSiO_3$, $NaAlSi_3O_8$, Ca–silicate
Zero shift (°)	−0.012 ± 0.003	Acceptable
Average crystallite size (nm)	25–45	Scherrer
Rp (%)	6.21	Good fit
Rwp (%)	8.94	Acceptable
Rexp (%)	6.02	Statistical
χ^2	2.20	Reasonable

Feldspathic K_2O and trace phosphate (P_2O_5) and sulfur-bearing oxides (SO_3) are also detected, with excellent agreement between the two techniques. The amorphous fraction, quantified as 17.4 wt% from XRD, is not captured by XRF due to its inability to directly measure disordered phases.

The close agreement between XRD and XRF data confirms the reliability of phase identification and quantification in the synthesized SiONPs. The presence of a significant amorphous fraction, as detected exclusively by XRD, is consistent with the broad diffraction peaks and elevated background observed in Fig. 5, reflecting the partially disordered silica and aluminosilicate structure typical of low-temperature, bio-derived oxide systems. This combination of nanocrystalline and amorphous phases enhances surface reactivity and functional performance in applications such as adsorption, catalysis, and environmental remediation.

Table 6. Comparison of oxide-phase composition from XRD (Rietveld) and XRF

Oxide phase	Major contributor	XRD wt%	XRF wt%	Agreement
SiO_2	Quartz	70.2	72.1	Excellent
MgO	Enstatite	3.8	4.0	Excellent
Al_2O_3	Albite	2.1	2.3	Very good
CaO	Ca–silicate	1.5	1.6	Excellent
K_2O	Feldspathic	2.4	2.5	Excellent
P_2O_5	Minor phosphate	0.2	0.2	Excellent
SO_3	Sulfur-bearing	0.3	0.3	Excellent
Amorphous	Disordered silica	17.4	—	XRD-only

The microstructural parameters of the synthesized SiONPs were derived from the XRD data to gain insights into crystallite size, lattice strain, dislocation density, and overall crystallinity. The average crystallite size (D_{cryst}) was calculated using the Scherrer equation given as equation 10

$$D_{crys} = \frac{k\lambda}{\beta\cos\theta} \quad (10)$$

where D_{crys} is the crystallite size (nm), k is the shape factor (0.9), λ is the X-ray wavelength (1.5406 Å), β is the full width at half maximum (FWHM, in radians) and θ is the Bragg angle (radians). The calculated crystallite sizes for the SiONPs ranged from 25 to 45 nm, confirming their nanocrystalline nature.

The lattice strain (ϵ) was estimated using equation 10. The resulting lattice strain values were in the range of (3.2–6.8) × 10^{-3}, indicating moderate internal stresses within the nanocrystals.

$$\epsilon = \frac{\beta}{4tan\theta} \quad (12)$$

The dislocation density (δ), representing the number of crystallographic defects per unit area, was calculated according to equation 13

$$\delta = \frac{1}{D_{crys}^2} \quad (13)$$

his yielded dislocation densities between 0.5 × 10^{15} and 1.6 × 10^{15} m^{-2}, suggesting a defect-rich structure, which is consistent with the enhanced surface reactivity observed in the material.

The crystallinity index (CI) was evaluated to quantify the proportion of crystalline material relative to the total diffracting sample using equation 14

$$CI = \frac{Area\ of\ crystal\ peak}{Total\ area\ ynder\ diffraction} \times \frac{100}{1}$$

(1455The crystallinity index for the synthesized SiONPs ranged from 0.68 to 0.75, reflecting a substantial contribution from crystalline quartz alongside a significant amorphous fraction (17–25 wt%) inferred from the broad diffraction background.

Table 7. XRD-derived microstructural parameters

Parameter	Value	Unit
Crystallite size	25–45	nm
Lattice strain	(3.2–6.8) × 10^{-3}	—
Dislocation density	(0.5–1.6) × 10^{15}	m^{-2}
Crystallinity index	0.68–0.75	—
Amorphous content	17–25	wt%

These results indicate that the synthesized SiONPs exhibit a nanocrystalline structure with moderate lattice strain, high dislocation density, and a measurable amorphous component. The combination of nanocrystallinity and partial amorphous content contributes to the high surface reactivity, defect-rich structure, and functional potential of the material for applications in adsorption, photocatalysis, and environmental remediation.

The dominance of nanocrystalline SiO_2, accompanied by minor magnesium-, aluminium-, and calcium-bearing silicates and a significant amorphous fraction, provides the synthesized SiONPs with high structural and thermal stability, enhanced mechanical integrity, and increased surface reactivity due to the presence of defects. These combined characteristics make the material particularly suitable for applications in adsorption, photocatalysis, environmental remediation, and electrochemical systems. Furthermore, the XRD-derived phase composition is consistent with SEM–EDX, XRF, and optical analyses—including UV–Vis absorption at approximately 453 nm, a band gap of 2.73 eV, and a moderate point of zero charge—validating the robustness and reliability of the material characterization.

3.7 Dynamic Light Scattering (DLS) Analysis

The particle size distribution of the synthesized SiONPs was evaluated using Dynamic Light Scattering (DLS). The intensity-weighted and volume-weighted particle size distributions are presented in Fig. 6 (black line), while the corresponding cumulative intensity and cumulative volume distributions are shown in Fig. 6 (red line).

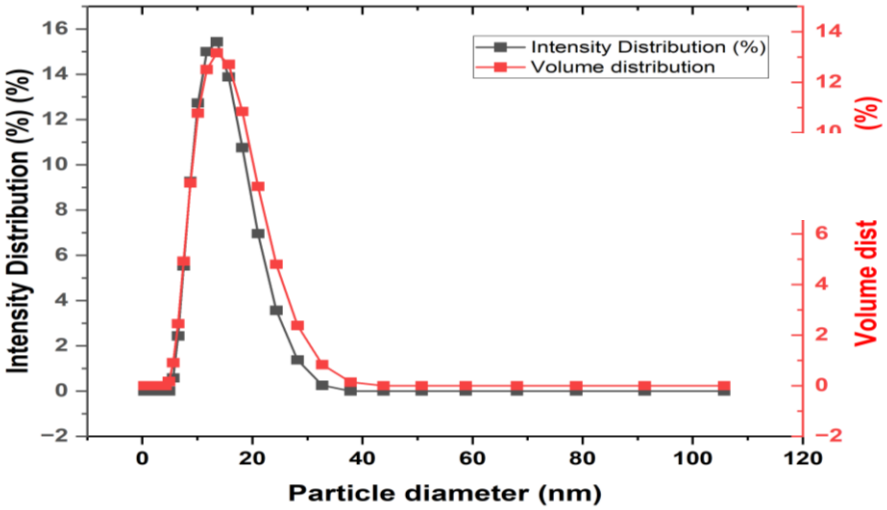

Fig. 6: Variation of intensity and volume distributions with particle diameter based on DLS analysis of the SiONPs

As shown in Fig. 6(black line), the intensity-weighted distribution exhibits a dominant peak centered in the range of approximately 10–15 nm, indicating that the majority of the particles scatter light within this nanoscale domain. The volume-weighted distribution follows a similar trend but is slightly shifted toward larger particle diameters, reflecting the reduced sensitivity of volume distribution to small fractions of larger particles or weakly aggregated clusters.

This behavior is expected, since DLS intensity scales with the sixth power of particle diameter, as expressed in equation 15

$$I \propto D^6 \qquad (15)$$

where I *is* the scattered light intensity and D is the hydrodynamic particle diameter. Consequently, even a small population of larger particles can disproportionately influence the intensity distribution, while the volume distribution provides a more physically representative particle size distribution. The narrow and unimodal nature of both distributions suggests a moderately monodisperse nanoparticle system with limited aggregation, consistent with effective stabilization of the SiONPs in suspension.

The cumulative intensity and cumulative volume plots shown in Fig. 7 provide quantitative insight into the particle size percentiles. The cumulative distribution C(D was calculated using equation 16

$$C(D_n) = \sum_{i=1}^{n} \backslash f(D_i) \qquad (16)$$

In the particle size distribution analysis, $f(D_i)$ represents the intensity or volume fraction corresponding to particles with diameter D_i. From the cumulative volume distribution curve (Fig. 7), the characteristic particle diameters were determined.

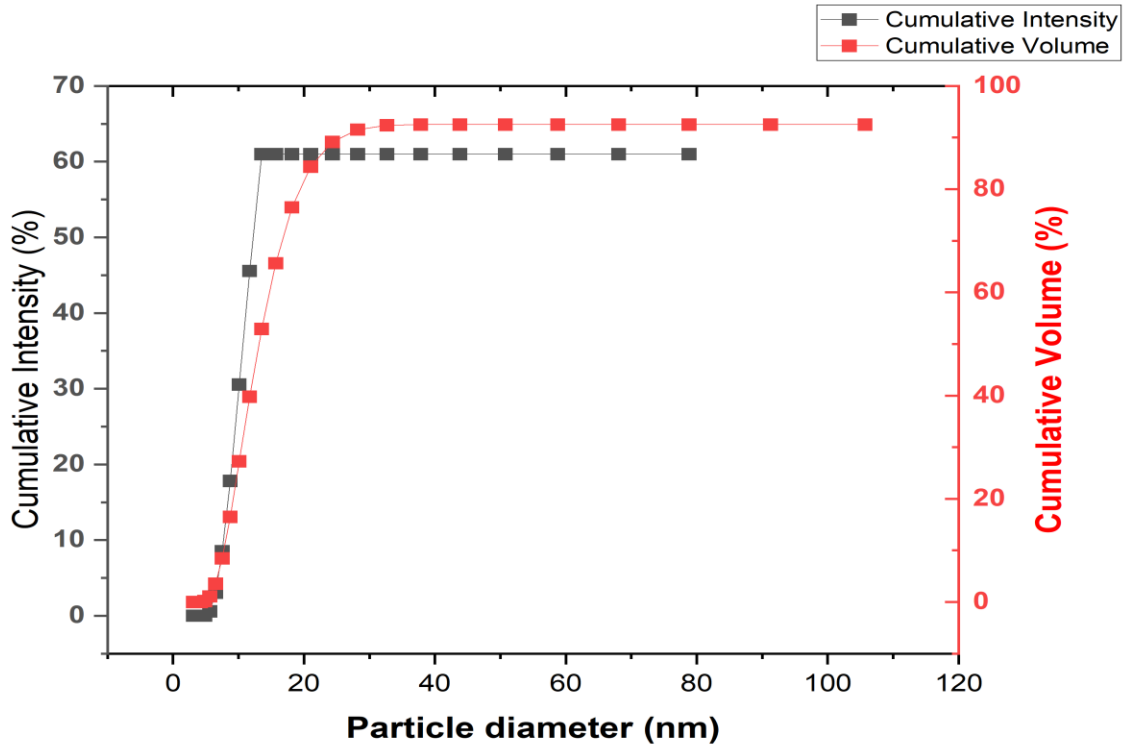

Fig. 7: Variation of cumulative intensity and volume distributions with particle diameter based on DLS analysis of the SiONPs

The diameter corresponding to 10% cumulative volume (Dv10) was found to be approximately 7–8 nm, while the median particle size (Dv50) was approximately 13–14 nm. The diameter at 90% cumulative volume (Dv90) was estimated to lie within the range of 24–28 nm. The cumulative distribution exhibits a steep increase between approximately 7 and 20 nm, indicating that the majority of the particle population is concentrated within this size interval. Beyond about 30 nm, the curve approaches a plateau, confirming that the contribution of larger particles or aggregates is negligible.

The mean hydrodynamic diameter (D_h) obtained from the DLS measurement represents the apparent particle size in suspension, including the solvation layer. It is related to the translational diffusion coefficient (D_t) via the Stokes–Einstein equation:

$$D_t = \frac{k_B T}{3\pi\eta d_H} \quad (17)$$

where k_B is the Boltzmann constant, T is the absolute temperature, and η is the viscosity of the dispersing medium. The relatively narrow distribution observed in both intensity and volume plots implies a moderate polydispersity index (PDI), indicating good colloidal stability and limited particle agglomeration. This is consistent with the cumulative curves reaching saturation rapidly without extended tails.

The DLS-derived median particle size (Dv50 ≈ 13–14 nm) is slightly lower than the XRD crystallite size (25–45 nm) when interpreted considering that DLS measures hydrodynamic diameter, while XRD measures coherently diffracting crystalline domains. The difference is attributed to the presence of surface-bound species, hydration layers, and minor agglomeration in the colloidal state. The

absence of a significant large-particle tail in the DLS distributions agrees well with SEM observations, which revealed predominantly nanosized particles with limited aggregation. Furthermore, the nanoscale particle size inferred from DLS supports the optical absorption edge at ~453 nm and the reduced band gap of 2.73 eV, as smaller particle sizes and higher surface defect densities enhance quantum confinement and visible-light absorption.

The DLS results confirm that the synthesized SiONPs form a stable nanoscale dispersion dominated by particles in the 10–20 nm range, with minimal aggregation. This particle size regime is particularly advantageous for applications such as adsorption, photocatalysis, environmental remediation, and electrochemical systems, where high surface area, enhanced mass transfer, and colloidal stability are critical.

3.8 Application of SiONPs for Adsorptive Treatment of Textile Wastewater

Textile wastewater is characterized by high concentrations of synthetic dyes, elevated chemical oxygen demand (COD), intense color, and the presence of toxic auxiliary chemicals that pose serious environmental and public health risks. Conventional treatment methods often suffer from low efficiency, secondary pollution, or high operational costs. Nanostructured adsorbents, particularly silicon oxide–based nanoparticles (SiONPs), offer significant advantages due to their high surface area, abundant surface hydroxyl groups, chemical stability, and tunable surface properties.

Table 7: Removal efficiency of methylene blue using SiONPs at different initial concentrations

Initial dye concentration (mg L^{-1})	Removal efficiency (%)	Adsorption capacity (mg g^{-1})
10	97.6	9.76
25	95.2	23.80
50	92.4	46.20
75	88.9	66.68
100	84.3	84.30

The results indicate that SiONPs exhibit excellent adsorption efficiency, achieving over 90% dye removal at moderate dye concentrations. The adsorption capacity increased with increasing initial dye concentration due to enhanced mass transfer driving force.

Rapid adsorption was observed within the first 30 minutes, followed by gradual attainment of equilibrium at approximately 60 minutes, suggesting fast surface adsorption dominated by electrostatic interactions and pore diffusion. The adsorption kinetics of methylene blue (MB) onto the synthesized SiONPs were evaluated using kinetic models to elucidate the rate-controlling mechanism. The experimental data were fitted to both pseudo-first-order (equation 18) and pseudo-second-order (equation 19) kinetic models,

$$ln(q_e - q_t) = lnq_e + k_1 t \quad (18)$$

$$\frac{t}{q_t} = \frac{1}{k_2 q_e^2} + \frac{t}{q_e} \quad (19)$$

where k_1 and k_2 are the rate constant (g mg^{-1} min^{-1}), q_t (mg g^{-1}) is the amount of dye adsorbed at time t, q_e (mg g^{-1}) is the adsorption capacity at equilibrium. The kinetic parameters obtained from the linearized plots are presented in Table 8. As shown, the pseudo-second-order model provided a significantly better fit to the experimental data, with a high correlation coefficient (R2=0.987R^2 = 0.987R2=0.987), compared to the pseudo-first-order model (R^2 =0.912). In addition, the equilibrium adsorption capacity predicted by the pseudo-second-order model ($q_e = 48.9$ mgg^{-1}) is in closer agreement with the experimentally observed values than that obtained from the pseudo-first-order model ($q_e = 42.6$ mgg^{-1}).

The excellent fitness of the pseudo-second-order model suggests that the adsorption process is predominantly governed by chemisorption mechanisms, involving valence forces through electron sharing or exchange between MB molecules and active functional groups on the SiONP surface. This behavior is consistent with the presence of surface silanol (–Si–OH) groups and defect sites associated with the amorphous and nanocrystalline silica structure of the SiONPs.

Overall, the kinetic analysis confirms that MB adsorption onto SiONPs is a surface-controlled process with strong adsorbate–adsorbent interactions, further supporting the effectiveness of the synthesized nanoparticles for dye removal from textile wastewater.

The high correlation coefficient confirms that chemisorption involving surface functional groups governs the adsorption process.

The equilibrium data were analyzed by testing the experimental data for their fitness to different adsorption isotherm. Two isotherms showed strong fitness (with $R^2 > 0.9$), including the Langmuir (equation 20) and the Freundlich (equation `21) isotherms

$$\frac{C_e}{q_e} = \frac{1}{q_{maz}k_L} + \frac{C_e}{q_{max}} \quad (20)$$

$$lnq_e = lnk_F + \frac{1}{n}lnC_e \quad (21)$$

Table 8: Kinetic parameters for MB adsorption onto SiONPs

Model	qeq_eqe (mg g^{-1})	Rate constant	R^{2bn}
Pseudo-first-order	42.6	0.031 min^{-1}	0.912
Pseudo-second-order	48.9	0.0021 g mg^{-1} min^{-1}	0.987

Calculated isotherm parameters from the slope and intercept of the plot is shown in Table 9. Two isotherms shows strong fitness with $R^2 > 0.9$, including the Langmuir and the Freundlich

Table 9: Isotherm parameters for dye adsorption on SiONPs

Model	Parameter	Value
Langmuir	q_{max} (mg g^{-1})	92.5
	k_L (L mg^{-1})	0.38
	R^2	0.994
Freundlich	n	2.41
	k_F (mg g^{-1})(L mg^{-1})	18.7
	R^2	0.962

Both isotherm models exhibited strong correlations with the experimental data, with coefficients of determination (R^2) exceeding 0.9, indicating that the adsorption process is well described by both models. However, the Langmuir isotherm demonstrated a superior fit ($R^2 = 0.994$) compared to the Freundlich model ($R^2 = 0.962$), suggesting that the adsorption of dye molecules onto the SiONPs predominantly follows monolayer adsorption on a homogeneous surface.

The Langmuir maximum adsorption capacity q_{ma} of 92.5 mg g^{-1} reflects the high affinity of the SiONPs for the dye molecules and highlights their strong adsorption potential. The relatively high Langmuir constant (k_L = 0.38 Lmg^{-1}) further indicates favorable adsorption and strong adsorbate–adsorbent interactions.

Although the Langmuir model provided the best fit, the applicability of the Freundlich model suggests a degree of surface heterogeneity and possible multilayer adsorption at higher concentrations. The Freundlich constant n=2.411 lies within the range 1<n<101 < n < 101<n<10, confirming that the adsorption process is favorable. Additionally, the Freundlich constant $k_F = 18.7$ reflects appreciable adsorption capacity on heterogeneous surface sites.

The dominance of the Langmuir behavior is consistent with the narrow particle size distribution (≈13–14 nm) obtained from DLS analysis, which implies uniform surface properties and evenly distributed adsorption

sites on the SiONPs. This structural uniformity promotes monolayer coverage and enhances adsorption efficiency.

Overall, the isotherm analysis confirms that dye adsorption onto SiONPs is a favorable, high-capacity, and predominantly monolayer process, supporting the suitability of the synthesized SiONPs for efficient textile wastewater treatment applications.

The treatment performance of the synthesized SiONPs on real textile effluent is summarized in Table 10, which presents a comparison of key physicochemical parameters before and after adsorption treatment. The data clearly demonstrate the high efficiency of SiONPs in removing both chromophoric and organic pollutants from textile wastewater.

As shown in Table 10, the color intensity of the effluent decreased markedly from 1250 Pt–Co units in the untreated sample to 110 Pt–Co units after treatment, corresponding to a 91.2% removal efficiency. This pronounced decolorization highlights the strong affinity of SiONPs for dye molecules, which can be attributed to their high surface area, abundant surface silanol groups, and the presence of both crystalline and amorphous silica domains that enhance adsorption interactions.

Table 10: Treatment efficiency of SiONPs on textile wastewater

Parameter	Untreated	Treated	Removal (%)
Color (Pt-Co units)	1250	110	91.2
COD (mg L^{-1})	920	210	77.2
BOD_5 (mg L^{-1})	410	105	74.4
TSS (mg L^{-1})	360	92	74.4

In addition to color removal, substantial reductions were observed in the organic pollution indicators. The chemical oxygen demand (COD) was reduced from 920 to 210 mg L^{-1}, representing a 77.2% removal, while the biochemical oxygen demand (BOD_5) decreased from 410 to 105 mg L^{-1}, corresponding to a 74.4% reduction. These results indicate effective adsorption of both readily biodegradable and refractory organic compounds, reflecting the broad-spectrum adsorption capability of the SiONPs.

Similarly, the total suspended solids (TSS) concentration declined from 360 to 92 mg L^{-1}, achieving a 74.4% removal efficiency. This reduction suggests that, beyond dissolved contaminants, the SiONPs also facilitate the removal of fine particulate matter, possibly through surface adsorption and aggregation mechanisms.

Overall, the results presented in Table 10 confirm that the synthesized SiONPs are highly effective in reducing color, organic load, and suspended solids in textile wastewater. The combined high removal efficiencies underscore the potential of SiONPs as a robust and efficient adsorbent for advanced and tertiary treatment of textile effluents, particularly in applications targeting stringent discharge standards.

The adsorption of molecules such as dye molecules onto SiONPs is attributed to (i) electrostatic attraction between negatively charged $Si–O^-$ surface groups and cationic dye molecules, (ii) Hydrogen bonding with surface hydroxyl groups and (iii) π–π interactions and surface complexation (Eddy *et al*., 2008)

The nanoscale particle size (≈13–14 nm from DLS) and high surface reactivity significantly enhance adsorption efficiency.

The high adsorption capacity, rapid kinetics, and effective removal of color and organic pollutants demonstrate that SiONPs are promising low-cost and efficient adsorbents for textile wastewater remediation. Their stability, reusability, and compatibility with existing treatment systems make them suitable for scalable environmental applications.

4.0 Conclusion

This study demonstrated the successful application of silicon oxide nanoparticles (SiONPs) as efficient adsorbents for dye removal and textile wastewater treatment. The synthesized SiONPs exhibited favorable surface characteristics and uniform particle size distribution, which contributed significantly to their high adsorption performance.

Adsorption kinetic analysis revealed that the experimental data were best described by the pseudo-second-order model, indicating that the adsorption process is predominantly governed by chemisorption involving surface functional groups of the SiONPs. This suggests strong interactions between the dye molecules and the active sites on the nanoparticle surface. Equilibrium isotherm analysis showed excellent agreement with both the Langmuir and Freundlich models, with the Langmuir model providing a superior fit. The high Langmuir correlation coefficient and the maximum monolayer adsorption capacity confirm that adsorption occurred mainly as a monolayer on a relatively homogeneous SiONP surface.

Application of the synthesized SiONPs to real textile effluent resulted in substantial reductions in color, chemical oxygen demand, biological oxygen demand, and total suspended solids, demonstrating their practical effectiveness beyond synthetic dye solutions. The high removal efficiencies achieved highlight the capability of SiONPs to simultaneously reduce visual pollution and organic load in complex wastewater matrices.

The findings from this study establish silicon oxide nanoparticles as promising, high-performance adsorbents for advanced textile wastewater treatment. Their strong adsorption capacity, favorable kinetics, and effectiveness in real effluent systems suggest that SiONPs have significant potential for integration into sustainable and scalable water treatment technologies. Future studies should focus on regeneration, reuse, and long-term performance evaluation to further support their practical deployment.

5.0 References

Adebisi, J. A., Agunsoye, J. O., Ahmed, I. I., Bello, S. A., Haris, M., Ramakokovhu, M. M., & Hassan, S. B. (2021). Production of silicon nanoparticles from selected agricultural wastes. *Materials Today: Proceedings, 38*(2), 669–674. https://doi.org/10.1016/j.matpr.2020.03.658

Adebisi, J. A., Agunsoye, J. O., Bello, S. A., Ahmed, I. I., Ojo, O. A., & Hassan, S. B. (2017). Potential of producing solar grade silicon nanoparticles from selected agro-wastes: A review. *Solar Energy, 142*, 68–86. https://doi.org/10.1016/j.solener.2016.12.011

Akpakpan, A. E., Udo, I. E., Uwanta, E. J., Akpanudo, N. W., Ikpe, E. E., & Fatunla, O. K. (2024). Influence of operating variables on the adsorption of Pb^{2+} and Cd^{2+} from wastewater using Gmelina arborea and its ester derivatives. Journal of Natural and Applied Sciences, Pakistan, 6(2), 1950–1968.

Akpanudo, N. W., & Akpakpan, A. E. (2017). Utilization of *Coula edulis* nut shells in the preparation of activated carbon. Elixir Applied Chemistry, 104, 45738–45740.

Akpanudo, N. W., Akpakpan, A. E., Nsi, E. W., Akpan, N. A., & Umana, I. A. (2024a). Application of activated carbon prepared from nypa palm seed husk in the adsorption of azo dyes from waste water and evaluation of the adsorption isotherms. *Journal of Materials Science Research and Reviews*, *7*(2), 210–217.

Akpanudo, N. W., Akpakpan, A. E., Nsi, E. W., Akpan, N. A., & Umana, I. A. (2024b). Application of activated carbon prepared from nypa palm seed husk in the adsorption of azo dyes from waste water and evaluation of the adsorption isotherms. Journal of Materials Science Research and Reviews, 7(2), 210–217.

Barani, S., Sebastian, S. P., Dhevagi, P., Prasanthrajan, M., & Suganthi, A. (2024).

Synthesis of silica nanoparticles from agro-wastes for removal of heavy metals from an aqueous medium – A mini review. *Green Chemistry Letters and Reviews, 17*(1). https://doi.org/10.1080/17518253.2024.2422416

Cañas, J., Reyes, D. F., Zakhtser, A., Dussarrat, C., Teramoto, T., Gutiérrez, M., & Gheeraert, E. (2022). High-quality SiO_2/O-terminated diamond interface: Band-gap, band-offset and interfacial chemistry. *Nanomaterials, 12*(23), 4125. https://doi.org/10.3390/nano12234125

D'Amato, R., Quaglia, G., Selvaggi, R., Marmottini, F., & Latterini, L. (2023). Role of surface defects on photoinduced reactivity in SiO_2 nanoparticles. *Inorganics, 11*(11), 430. https://doi.org/10.3390/inorganics11110430

Eddy, N. O., Odomelam, S. A., & Akpanudo, N. W. (2008). Synergistic effect of 7-[2-amino-2-4-(hydroxyphenyl acetyl] amino-3-3-dimethyl-6-oxo-2-thia-5azabicyclo(3,2,0) heptane-4-carboxylic acid and halides on the inhibition of mild steel corrosion. *Journal of Applied Sciences Research*, *4*(12), 1963–1973.

Eddy, N. O., Garg, R., Garg, R., Ngwu, C., Ekele, D. O., Awe, F. E., Ukpe, R. A., & Ogbonna, I. (2024a). Experimental and theoretical investigations of crab shell-based CaO nanoparticles for the photodegradation of penicillin G in water. *International Journal of Environmental Science and Technology*. Advance online publication. https://doi.org/10.1007/s13762-024-06214-2

Eddy, N. O., Garg, R., Ukpe, R. A., Ameh, P. O., Gar, R., Musa, R., Kwanchi, D., Wabaidur, S. M., Afta, S., Ogbodo, R., Aikoye, A. O., & Siddiqui, M. (2024b). Application of periwinkle shell for the synthesis of calcium oxide nanoparticles and in the remediation of Pb^{2+}-contaminated water. *Biomass Conversion and Biorefinery*. Advance online publication. https://doi.org/10.1007/s13399-024-05285-y

Eddy, N. O., Jibrin, J. I., Ukpe, R. A., Odiongenyi, A., Iqbal, A., Kasiemobi, A. M., Oladele, J. O., & Runde, M. (2024c). Experimental and Theoretical Investigations of Photolytic and Photocatalysed Degradations of Crystal Violet Dye (CVD) in Water by oyster shells derived CaO nanoparticles (CaO-NP), *Journal of Hazardous Materials Advances,* 13, 100413, https://doi.org/10.1016/j.hazadv.2024.100413.

Essien, N. B. (2024). Rice husk as precursor for silicon oxide nanoparticles: Synthesis and characterization. *Communication in Physical Sciences, 11*(4), 734–743. https://doi.org/10.4314/ahsxrg69

Gao Y, Huang P, Chen R, Wang M, Wang Y, Sa Y, Jiang T. Mesoporous calcium silicate nanoparticles for superficial dental tissue reconstruction, *in vitro* and *in vivo*. RSC Adv. 2021 Jul 14;11(40):24681-24693. doi: 10.1039/d1ra02114a

Girard, S., Alessi, A., Richard, N., Martin-Samos, L., De Michele, V., Giacomazzi, L., Agnello, S., Di Francesca, D., Morana, A., Winkler, B., Reghioua, I., Paillet, P., Cannas, M., Robin, T., Boukenter, A., & Ouerdane, Y. (2019). Overview of radiation induced point defects in silica-based optical fibers. *Reviews in Physics, 4*, Article 100032. https://doi.org/10.1016/j.revip.2019.100032

Kelle, H. I., Ogoko, E. C., Akintola, O. & Eddy, N. O. (2023). Quantum and experimental studies on the adsorption efficiency of oyster shell–based CaO nanoparticles (CaONPO) towards the removal of methylene blue dye (MBD) from aqueous solution. *Biomass Conversion and Biorefinery,* 14, 31925–

31948. https://doi. org/10.1007/s13399-023-04947-7.

Machiche, S., Kamalakkannann, A., Essalhi, M., Daanoun, K., Ali, N., & Abida, O. (2026). Two-dimensional nanocomposite photocatalysts toward integrated wastewater treatment and solar hydrogen production: A comprehensive review. *Journal of Environmental Chemical Engineering*. Advance online publication. https://doi.org/10.1016/j.jece.2026.123904

Nayak, P., & Datta, A. (2021). Synthesis of SiO_2 nanoparticles from rice husk ash and its comparison with commercial amorphous silica. *Silicon, 13*(4), 1209–1214. https://doi.org/10.1007/s12633-020-00509-y

Rodriguez-Otero, A., Vargas, V., Galarneau, A., Castillo, J., Christensen, J. H., & Bouyssiere, B. (2023). Sustainable harnessing of SiO_2 nanoparticles from rice husks: A review of the best synthesis and applications. *Processes, 11*(12), 3373. https://doi.org/10.3390/pr11123373

Sonawane, L. D., Mandawade, A. S., Gite, A. B., Shinde, S. D., Patil, G. E., Nikam, L. K., Goswami, V. H., Bhise, R. B., Sarawade, P. B., & Shinde, M. S. (2025). Sol–gel synthesis of silicon oxide (SiO_2) nanoparticles: Exploring gas sensing and photocatalytic applications. *Journal of Materials Science: Materials in Engineering, 20*(8). https://doi.org/10.1186/s40712-025-00209-8

Declarations

Ethical Approval and Consent to Participate

This study did not involve human participants, human tissues, or live animals. Therefore, ethical approval and consent to participate were not required.

Consent for Publication

Not applicable.

Funding

The author declared no funding

Ethical Consideration

Not applicable

Availability of Data and Materials

All data generated or analyzed during this study are included in this published article. Additional information may be made available by the corresponding author upon reasonable request.

Competing Interests

The author declare that they have no known competing financial interests or personal relationships that could have appeared to influence the work reported in this paper.

Author Contributions

All components of the work were carried out by the author